J. Appl. Comput. Mech., 9(4) (2023) 1093-1106
DOI: 10.22055/jacm.2023.43103.4028

ISSN: 2383-4536
jacm.scu.ac.ir

Shahid Chamran University of Ahvaz

Journal of Applied and Computational Mechanics

Research Paper

Study of the Vibration Characteristics of SA 330 Helicopter Planetary Main Gearbox

Adebayo A. Ogundare[1], Sunday J. Ojolo[1], Adekunle Adelaja[1], David Mba[2], Linghao Zhou[3], Xiaochuan Li[4]

[1] Department of Mechanical Engineering, University of Lagos, Akoka, Lagos, Nigeria,
Email: aogundare@unilag.edu.ng (A.A.O.); sojolo@unilag.edu.ng (S.J.O.); aadelaja@unilag.edu.ng (A.A.)

[2] Research, Knowledge Exchange and Enterprise, University of the Arts London, London, UK, Email: d.mba@arts.ac.uk

[3] MIR Section, NDE Group, MIR Section, NDE Group, TWI Limited, London, UK, Email: linghao.zhou@twi.co.uk

[4] School of Electrical Engineering and Automation, Hefei University of Technology, Hefei, China, Email: xiaochuan.li0309@gmail.com

Received February 23 2023; Revised May 19 2023; Accepted for publication June 23 2023.
Corresponding author: A.A. Ogundare (aogundare@unilag.edu.ng)

Abstract. The planetary gear sets find application in the final stages of the helicopter transmission system. Unlike the single axis gear, the planetary gears have complex structural arrangement and unique operational characteristics which makes diagnosis of incipient fault much more challenging with planetary gears compared to the single axis gear. This study provides a background for effective planetary bearing fault analysis in an SA330 Super-Puma Helicopter Main gearbox by studying the characteristic of the planetary stage and investigating some prominent frequency components which are vital to fault feature extraction. Vibration data of healthy and faulty conditions at varying load regimes from a seeded fault experiment were captured. The analysis of the vibration transmission paths and the signal amplitude in the time and frequency domain provide the basis for the determination of the best signal quality. Eight transmission paths affecting the signal energy were established however, the shortest path to the radial direction of the faulty bearing assures better signal gain. The gear mesh frequencies and harmonics of the planetary stages are suppressed by the high amplitude frequencies of the forward, aft and bevel reduction gears. The impulsive carrier frequency at high speed has a strong correlation with gear-related frequencies. Though the fault frequencies can be traced in some instances, it is mostly dominated in the spectrum because of the gear-related frequencies and amplitude modulation of the planetary stages. This work enhances the planetary bearing fault extraction.

Keywords: Planetary bearing; seeded fault; vibration; frequency, harmonics.

1. Introduction

The challenge of the planetary gear tray is a combination of the harsh operational environment, the arrangement and relationship of the structural members, and its unique vibration characteristics. This gear arrangement finds application in high-power machinery to provide coaxial gear reduction [1], with the added advantage of high load-bearing capacity, transmission ratio and transmission efficiency [2]. By design and application, they are exposed to rough operations characterized by heavy impact loading that make the system susceptible to failures.

The arrangement of the system is structured such that several planet gears on a planet carrier rotate about their own constantly changing centers while revolving around a centered sun gear and within an annulus ring gear [3, 4] to achieve a reduced output speed through the planet carrier. The planets experience epicyclic motion as they orbit around the sun gear [5]. The planet gears may be made to revolve around the rotating sun gear about its center while the ring gear is fixed, or the sun gear is fixed while the planet gear revolve within a rotating ring gear about its own centers or a stationary planetary carrier while the sun gear and ring gear rotates within and around the planet gears [6]. For each arrangement, there are two possible inputs and outputs. The peculiar behavior of the dynamic response and vibration signature of the epicyclic gear tray has attracted numerous interests and research. Studies [7-13] have shown that the individual planets gears operate at the same speed and load, and exhibit similar vibration, but with different and changing meshing phases as they mesh with the ring and sun gear. Thus, a fixed sensor measures a periodic amplitude-modulated vibration signal as each planet rotates past the sensor. The modulated signal exhibits naturally occurring sidebands in the frequency spectrum, both in a healthy and faulty component. Moreover, the constantly changing meshing phases alter the dominant frequency component such that the vibration signature in the planetary system is asymmetric about the gear meshing frequency and its integer harmonics [14]. The complex structural arrangement also imposes multiple variable vibration transmission paths. The constantly changing centers and meshing phases of the planet gear change the fault location constantly

Published online: June 30 2023

and result in a multiple of constantly changing and variable time variant transmission paths. There is a possibility of interference between the multiple transmission paths. The vibration energy transmission through oil is deterred by the large energy noise of the structural components and is assumed negligible [15]. Two time-variant transmission paths and four time-invariant transmission paths from the fault location to the accelerometer position in a single-stage planetary drive train component [13]. The gear ratio of the ring and planet gears are not always an integer and could suppress the vibration energy [1]. All the scenarios above, put together, suppressed the sideband produced by the dominant frequency component containing information about the health characteristics hidden in the signal and is further deteriorated by the design peculiarities and the environment of its application.

The use of Vibration Health Monitoring (VHM) for Machine Condition Monitoring (MCM) plays a vital role in the Health and Usage Monitoring System (HUMS) in ensuring helicopter safety and reliability. The HUMS-VHM is a data-driven approach. Several experimental approaches have been reported in literature to address the problem of fault location and size, sensor location and specification, operational speed, and load variation, with numerous studies investigating incipient fault in the Main Gearbox (MGB) in a laboratory scale to study the effectiveness of the HUMS condition indicators for fault identification [16]. In run-to-failure testing of an oil-cooler helicopter bearing in a miniature experimental test rig, a seeded corrosion fault in the bearing inner race eventually resulted in spall damage [17]. In a seeded fault experiment [18], spalling in a planet gear of single stage planetary reduction gearbox with a reduction ratio of 3.84:1 was investigated at the University of Maryland transmission test rig. Vibration data from an accelerometer to fiber optic strain sensor band mounted on the ring gear in the planetary stage of an OH-58C Bell Helicopter transmission at the NASA Glenn research test facility was investigated [19]. The strain sensor was reported to suffer decreased damage sensitivity at low torque levels and was unable to detect pitting in some components of the planetary stage. Investigation of spalls and cracks in the planet, sun and ring gear tooth using vibration separation techniques have been recorded in the literature [11]. Studies such as [20] provides guidelines on accelerometer mounting and specifications. The study also investigates seeded fault in the outer race of a planetary bearing with rectangular geometry of 10 mm and 30 mm in length for the minor and major fault, respectively, and a depth of 0.3 mm in both cases. Irregular fault surface is recommended by [21]. Earlier work on measured vibration data was carried out by [22] on a single-engine two-stage reduction gearbox of OH-58A helicopter main rotor transmission under varying torques and speed conditions at NASA Lewis transmission test stand. Seven accelerometers mounted at various locations was used on the transmission with orientation to capture possible transmission path in the vertical, transverse, longitudinal and 450 transverse-longitudinal. The same data was used by [23]. Numerous seeded fault tests were performed by [24] at the NAWCAD test cell facility, Trenton, NJ, to support Helicopter Integrated Diagnostic System (HIDS) program for SH-60 main transmission and investigate gear tooth breakage. An investigation by The U.S. Army Aviation Engineering Directorate, Aeromechanics Division on healthy and faulty vibration data from an H-47 swashplate bearing operated was carried out at several simulated flight conditions and steady flight condition over a 24-hour run on a specialized swashplate test rig located at Boeing Helicopters, Philadelphia [25]. In a run to failure experiment [26]. a gear tooth on the input spiral bevel pinion drive of a Bell OH-58 main rotor gearbox was notched and run for an extended period at several over-torque conditions in a transmission test rig to aid the propagation of the inserted fault until the tooth fracture in a spiral bevel gear. The dimensions of the seeded fault are 2.5 mm width, 0.13 mm length and 0.13 mm depth for the minor fault, while the major faults are 3 mm width, 0.54 mm length and 2 mm depth. A review of HUMS in the helicopter MGB [27] summarized the current practices for sensors application, data acquisition, monitoring and analysis and stressed the importance of maintaining data integrity for effective HUMS performance. Guidelines for the use of sensors was provided [28] while reviewing sensor requirements for health management. It was recommended that sensors should be reliable to work in harsh operating condition and high temperatures. For the economy of space, the importance of a single sensor that is capable of measuring vibration in multiple axes is crucial. The vibration energy of the fault signal is usually low and masked with noise, which should require an accelerometer sensor with high sensitivity. However, high sensitivity could saturate the output signal and reduce the dynamic measuring range considerably [29]. A comparison of the vibration data of UH-60 Black Hawk helicopters in a test stand and helicopter flight regime collected through an onboard commercial HUMS-Vibration management Enhancement program (VMEP) to was carried out to monitor pitting in the bearing races, cages and rolling bearing [30]. The difference in the environment, undefined limitations, and constraints of a test stand resulted in a significant difference in dynamic response. Attempts have been made to accommodate the variable load and speed conditions in the seeded fault test rig replicating, the helicopter flight regime and capture a maximum signal gain at low torque [31, 32].

Studies have shown that not much work has been done on planetary bearing diagnostics compared to gear [33]. The few works on bearing have been largely on single axis gear assembly. Earlier efforts to diagnose planetary faults have focused mainly gear faults, and most studies on bearing faults considered a fairly large fault size which might be too much for incipient fault initiation and propagation in a planetary bearing. Majority of the planetary bearing diagnostics are either drivetrain simulator [10, 34, 35], model-based approach or simulated data [36-38] which in most cases cannot replicate the actual field operating conditions. Few studies have adopted planetary bearing under varying load and speed regime to replicate the operational environment of the planetary gearbox in an experiment test stand [6]. This study considers a unique fault size in the 2nd planetary stage of an operational helicopter MGB under varying load and speed regime. The study focusses on the acquisition and choice of quality data. A novel analysis on the choice of the quality data for fault analysis as a foundation for the further fault diagnostics was caried out. The study also investigates the effect of the transmission paths, the carrier frequency and some prominent frequency components on the signal and future diagnostics.

2. Material and Methods

2.1 Seeded Fault Test in SA 330 Helicopter MGB

This study examines experimental vibration data from an operational commercial helicopter MGB in a test rig located at Cranfield University. The rig is adaptable to drive the MGB and provides varying load and speed conditions to replicate the field operating environment. The MGB is a Category A Super Puma SA330 helicopter MGB with two engine inputs to ensure optimum operational performance and continuous safe flight operation in the event of engine failure. The SA330 MGB is a speed reduction unit designed with an output speed of 265 rpm at an overall speed reduction of 68:1and comprises the forward reduction (FRG) stage, aft reduction gear (ARG) stage, bevel reduction gear (BRG) stage, 1st planetary stage and the 2nd planetary stage. The main rotor of the helicopter is connected to the MGB through the 2nd planetary stage output shaft.

The test rig is an assembly of several units consisting of two high-speed direct current (DC) motor connected in series to provide adequate initial drive speed; a speed-increasing gearbox for multi-stage speed acceleration, and an adjustable load absorption dynamometer mounted on the output shaft of the 2nd epicyclic stage of the MGB. The twin D.C Motors replace the engine and provide a combined maximum speed/ power of 3000 rpm/ 350 kW increased to 17842 rpm/ 293 kW through the speed increasing gearbox to drive the MGB. The dynamometer replaces the helicopter's main rotor and provides the desired loading effect. Each of the planetary stages comprises a fixed ring gear, a fixed axis sun gear, multiple numbers of planets with moveable axis and a planetary carrier plate attached to the planetary gears. Both stages are designed as a fixed ring gear system with the ring gear machined into the internal casing of the MGB, thus, the angular speed of the ring gear is zero. For the 1st planetary gear stage, the number of teeth for the sun gear, ring gear and planet gears are 62, 130 and 34, respectively, while that of the 2nd planetary stage are 68, 130 and 31, respectively. Each of the planets has a bearing inserted into it to aid its motion. Details of the planetary bearing and rolling elements are shown in Table 1.

2.2 The seeded fault test procedure

The emphasis of this study is on monitoring the planetary stages of the MGB; hence, the two aft module outputs were left idle. Likewise, since the twin helicopter engine does not run simultaneously, a single power source from the high input speed of the twin DC motor through the speed reduction gearbox provides the drive for the MGB through one of the forward reduction gear modules.

2.3 Preliminary test

The difference in the environmental factors in the test stand and the field that can limit the performance of diagnostics [30]. Hence, it is essential to understand the environment in the field application and apply the same to the test stand experiment. Therefore, preliminary tests were conducted before the seeded fault test to ensure that the test stand could replicate the field environment. This test was conducted under no-fault conditions to ensure that the entire test rig function optimally and to prevent any anomalies that might affect the outcome of the experiment. The rig was operated under various load conditions ranging from 100 kW to 275 kW and input speed ranging from 10,000 rpm to 17,842 rpm to ensure optimal functionality and performance of all individual components and sub-components of the test rig. A full lubrication test was also carried out on the MGB under various load conditions ranging from 100 kW to 275 kW and input speed ranging from 10,000 rpm to 17,842 rpm to monitor the thermal distribution and the rate of thermal growth within the planetary stage of the MGB. This test ensured thermal equilibrium of the component parts within the MGB and helped to forestall excessive temperature from affecting the performance of the piezoelectric accelerometers. Moreover, a combined run of dry and mist lubrication tests was also carried out to make provision for emergency lubrication under no lubrication in the event of a failed lubrication system. The data acquisition system was also tested to ensure correct and efficient data collection under a load of 150 kW with no fault condition. During the preliminary test, necessary adjustments were made to ensure the functional relationship and shaft alignment of all the individual components of the rig and the MGB.

2.4 Test conditions

The seeded defect test was conducted under different loading and speed conditions. A minimum speed and load condition of 14000 rpm at 100 kW, which is the operating condition of a typical helicopter under the idle condition on the ground before take-off as the benchmark for minimum operating conditions have been recommended [29]. The maximum operating condition of a high-speed DC motor, 17842 rpm, was used to benchmark the maximum speed at 16000 rpm. The seeded fault experiment was conducted for the baseline, mild fault, and severe fault condition under 14000 rpm/100 kW, 14000 rpm/180 kW, 16000 rpm/100 kW and 16000 rpm/180 kW speed and load regime. In-between test check was carried out after different speed and load conditions and the vibration data were checked from time to time to ensure the data integrity. The planetary bearings have to be replaced at the end of each health condition allowing an interval of different days in-between tests to dissemble the MGB and planetary bearings, replace the planetary bearings and reassemble the MGB, and still ensure that functional and safe operating conditions are maintained.

2.5 Seeded bearing defect

The incipient fault was seeded in one of the 2nd planetary bearing outer races. Two types of fault conditions, the mild and severe fault, were seeded and investigated against the baseline condition with no fault. For each type of fault condition, a planet was removed from the 2nd planetary stage and the bearing was dissembled for the incipient fault to be inserted using mechanical tools. The width of the fault used in this study is quite unique and small compared to the fault width used other studies [29], where seeded fault widths of 10 mm and 30 mm are used for the mild and severe fault, respectively. In this study, it is ensured that the incipient mild fault is not more than half of the outer race length while the severe fault is inserted to cover the entire width of the outer race. Figure 1 shows a dismantled planetary gear and bearing, and the dimensions of the seeded fault for the mild and severe faults.

Table 1. Planetary bearing and rolling elements.

Planetary stage	Number of gears	Number of bearings	Number of rolling elements
1st	8	8	17
2nd	9	9	13

(a) (b) (c)

Fig. 1. Illustration of gears showing the (a) dissembled planetary gear and bearing (b) mild fault size (c) severe fault size.

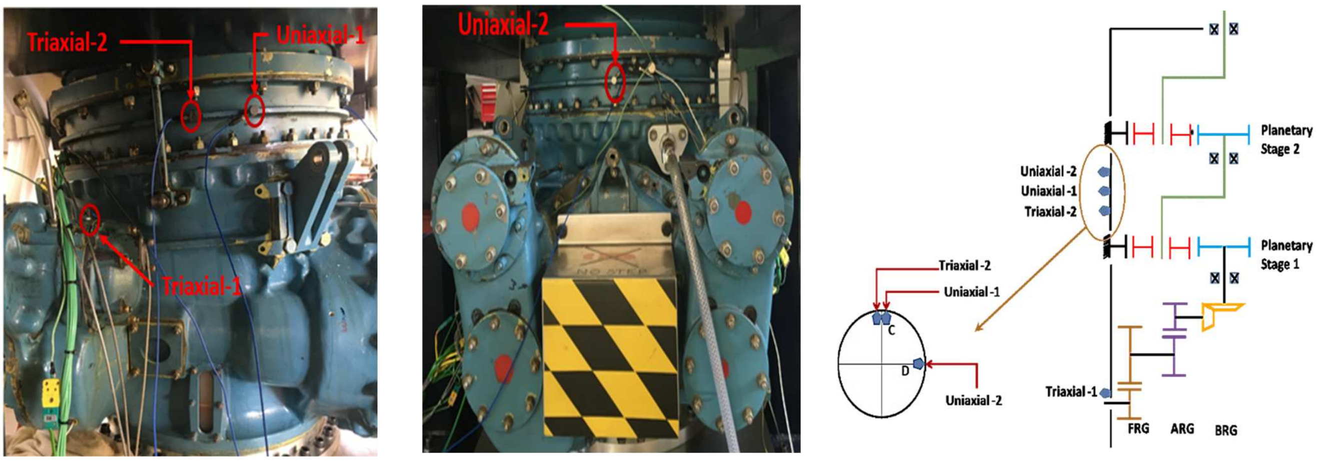

(a) (b) (c)

Fig. 2. Illustration of accelerometer's positions showing (a) side view (b) rear view (c) accelerator orientation.

2.6 Data acquisition

For efficient data acquisition, the choice and location of sensors are essential, especially in a complex gear arrangement like the SA 330 used in this study. Guidelines on the choice and positioning of accelerometers for the acquisition of vibration data in HUMS application have been suggested in the literature [22, 27-29]. Based on these guidelines, two uniaxial and two triaxial piezoelectric accelerometers were installed on the SA 330 MGB to avoid incurring the cost of adding extra accelerometers which may no longer be cost-effective and could also obstruct moving parts in the MGB. The triaxial accelerometer captures all three axes so that the sensitive axis of the piezoelectric accelerometer can be aligned with the axis where the vibration signal is predominant. Triaxial accelerometer 1 was installed at the input to the planetary stage as recommended by [39], while triaxial accelerometer 2 was installed in between the 1st and 2nd planetary stage to capture the critical drive train components and to be to as practically close as possible to the part intended to be monitored. Uniaxial accelerometers 1 and 2 were also installed in between the 1st and 2nd planetary stages but at 90° to each other. All the accelerometers are positioned such that the orientation of the sensitive axis is aligned with the predominant axis of the vibration signal to be measured. This ensures that no predominant vibration axis is neglected and clear energy transmission paths from the specific components being monitored are not obstructed. Small sized uniaxial and triaxial accelerometers were used to avoid interference with the mechanical structures of monitored components in the MGB. The triaxial accelerometers can capture vibration data in three directions and afford the luxury of using less accelerometers to economize space around the monitored component and prevent obstruction of the transmission paths. The uniaxial and triaxial accelerometers used are PCB 356A43 and PCB 352C03 hexagonal head and externally threaded for ease fastening to the MGB case. The accelerometers have a sensitivity of 10 mV/g and a measuring range of 500 g pk. For each health condition for the varying load and speed regime, the vibration data was recorded over a period of 20 seconds and sampled at 25600 Hz. The locations and orientations of the accelerometer's positions are shown in Fig. 2.

3. Theory and Calculations

The output speed of the 2nd planetary stage, which is the 2nd planetary carrier speed, is the overall output speed of the MGB. The output speed of the forward reduction gear module, N_{OF}, aft reduction gear module, N_{OA}, bevel gear module, N_{OB}, 1st planetary module, N_{O1} and 2nd planetary module, N_{O2} are given in Eqs. (1) to (5):

$$N_{OF} = \frac{N_i}{R_F} \tag{1}$$

$$N_{OA} = \frac{N_i}{R_F R_A} \tag{2}$$

$$N_{OB} = \frac{N_i}{R_F R_A R_B} \tag{3}$$

$$N_{O1} = \frac{N_i}{R_F R_A R_B R_{p1}} \tag{4}$$

$$N_{O2} = \frac{N_i}{R_F R_A R_B R_{p1} R_{p2}} \tag{5}$$

where N_i is the input speed from the engine, R_F, R_A, R_B, R_{p1} and R_{p2} are the gear transmission ratio of the FRG, ARG, BRG, and the 1st and 2nd planetary stage, respectively.

The fundamental gear mesh frequency (GMF) of a single axis gear may be expressed according to Ref. [40]. The GMF of the FRG, ARG and BRG and are given in Eqs. (6) to (8):

$$GMF_F = N_i Z_{PF} \tag{6}$$

$$GMF_B = N_i \frac{Z_{PF}}{Z_{SF}} Z_{PA} = N_I R_F Z_{PA} \tag{7}$$

$$GMF_B = N_i \frac{Z_{PF}}{Z_{SF}} \frac{Z_{PA}}{Z_{SA}} Z_{PB} = N_I R_F R_A Z_{PB} \tag{8}$$

where Z_{PF}, Z_{PA} and Z_{PB} are number of pinion teeth on the FRG, ARG and BRG respectively, Z_{SF} and Z_{SA} are the number of spur teeth on the FRG and ARG, respectively.

The fundamental GMF of the planetary stages, F_P and their integer harmonics, H_i was determined as shown in Eq. (9) and (10) and investigated in the vibration frequency spectrum. See Table 3 for a summary of the planetary stages GMF and the integer harmonics of the 1st and 2nd planetary stages:

$$F_P = Z_r N_o = Z_p N_P \tag{9}$$

$$H_i = n_i F_p, \quad (i = 1,2,3,\ldots,n) \tag{10}$$

where Z_r and Z_p are number of teeth on the ring gear and number of teeth on a planet gear respectively, while N_o and N_P are the speed of the planet carrier and the planet gear, respectively. n_i is the index number of the planetary gear. The transmission ratio, output speed and the GMF of all the reduction stages are summarized in Table 2. The overall speed reduction is 68: 1.

The vibration signal is analyzed with the Fast Fourier Transform (FFT) using MATLAB. The frequency spectrum was investigated for planet modulations, a common phenomenon with the planetary gear train. The dominant frequency components of the single-axis gears and planetary stages and the effect of the GMF of the single-axis gears in the frequency spectrum that could affect characteristics feature extraction were investigated. The carrier frequency, F_C is an essential factor for bearing envelope analysis in the selection of the demodulating frequency band for effective fault extraction in bearing. The bearing signal carrier frequency otherwise known as resonance frequency [41], bounded by a region of demodulating bandwidth is identified as the peak frequency of a bell shape curve in the frequency spectrum around an approximate value about halve of the sampling frequency, f_s as shown in Eq. (11). The carrier frequency should have no strong correlation with the gear mesh related frequencies and should be within the region of 12800 Hz. The carrier frequency was investigated for all the speed and load regime:

$$f_s \cong 2F_C \tag{11}$$

The ball pass frequency of the outer race (BPFO) is expressed in Eq. (12). In the signal spectrum the BPFO is modulated by the planetary carrier speed of the planetary stage where the fault originates. The lower (L_S) and upper (U_S) sideband modulation of the BPFO by the 2nd stage epicyclic carrier speed are expressed in Eq. (13) and (14), respectively:

$$BPFO = 5.2235 N_P \tag{12}$$

$$L_S = BPFO - N_{O2} \tag{13}$$

$$U_S = BPFO + N_{O2} \tag{14}$$

Table 2. Transmission ratio and output speed of the reduction stages.

Stages	p	ARG	BRG	1st Planetary	2nd Planetary
Z_B	23	35	22	-	-
Z_A	66	57	45	-	-
Z_P	-	-	-	34	31
Z_S	-	-	-	62	68
Z_r	-	-	-	130	130
R	2.81:1	1.63:1	2.05:1	3.1:1	2.91:1
N_O (Hz)	83.04	50.94	24.85	7.93	2.714
GMF (Hz)	5400.4	2863.85	1105.35	1022.27	350.65

Table 3. Integer harmonics of the 1st and 2nd Planetary Stage.

Harmonics	1st planetary stage (Hz)	2nd Planetary stage (Hz)
1st	1022.27	350.65
2nd	2044.54	701.3
3rd	3066.81	1051.95
4th	4089.08	1402.6
5th	5111.35	1753.25
6th	6113.62	2103.9
7th	7155.89	2454.55
8th	8178.16	2805.2
9th	N/A	3155.85

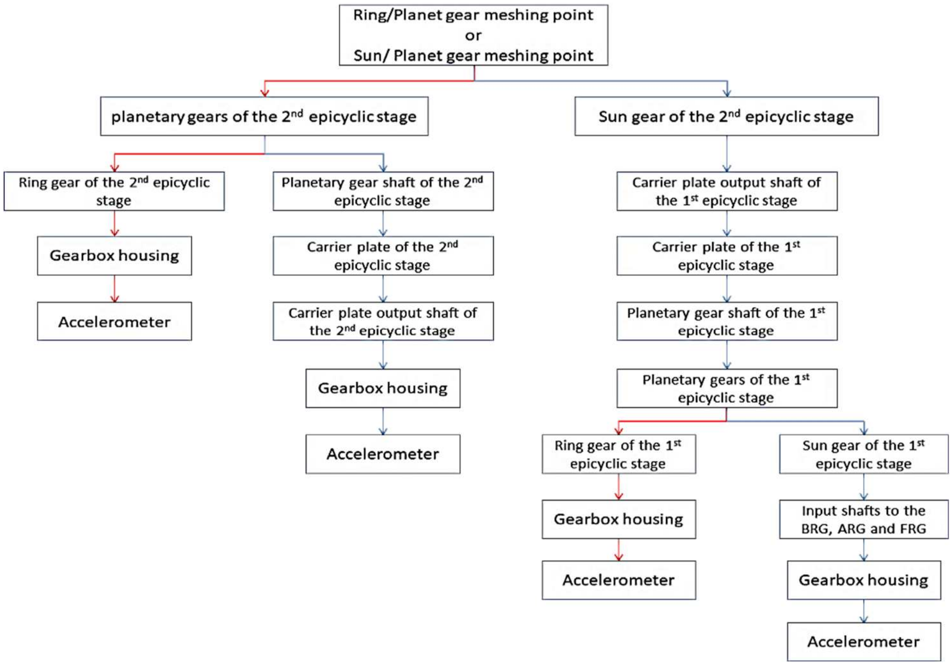

Fig. 3. Vibration transmission paths of the SSA 330 MGB.

4. Results and Discussion

The data was collected at 14000 rpm/100 kW, 14000 rpm/180 kW, 16000 rpm/100 kW and 16000 rpm/180 kW regime from the SA330 helicopter MGB for the baseline condition, mild fault, and severe fault condition over a period of 20 seconds and sampled at 25600 Hz. A key factor in the investigation fault for HUMS-VHM is the quality and integrity of the data used in diagnosis. The data acquired from the four accelerometers were investigated for the sensitive axis that would be most beneficial for further analysis and fault diagnosis. Vibration energy transmission path, signal strength in the time domain and frequency spectrum of the vibration signal were the three criteria investigated to determine the sensitive axis of the sensors.

4.1 Vibration energy transmission path

Figure 3 summarizes the transmission paths. The vibration transmission paths are taken with respect to the fault location in 2nd planetary stage to the accelerometer position. A total of eight possible transmission paths, of which four are time variants and the other four are time invariant, are visible from the accelerometers.

The ring gear and the accelerometers are fixed to the gearbox housing. The source of the vibration is the meshing point of the 2nd planetary stage sun with the planet gear where the seeded bearing fault is inserted, and the meshing point of the ring gear with the planet gear where the seeded bearing fault is inserted. The sun-planet gear meshing point has four transmission paths, while the ring-planet gear meshing point also has four transmission paths. The time invariant transmission paths are the paths from the vibration source of the planet-sun or planet-ring gear meshing point through the gear shafts only to the MGB housing. The time variant energy transmission paths are the paths from the vibration source of the planet-sun or planet-ring gear meshing point through the planet gear and the ring gear of the 1st or 2nd epicyclic stage to the MGB housing. The time variant transmission path is a direct path from the vibration source on the planet gear to the ring gear but have a variable position to the fixed accelerometer since the vibration source changes position as the planet gear rotates and revolves about the axis of the sun gear and meshes with the ring gear. Hence, the vibration energy transmission varies with time as the planet moves past and away from the fixed accelerometer. The time variant paths, as shown in Fig. 3, are paths through the ring gear, unlike the time invariant paths that must travel through several structural components in the MGB and through the sun gear shaft to get to the accelerometer installed on the MGB housing. Two out of the four-time invariant paths are a blend of the time variant and invariant paths. Each of the accelerometers collect data from all the transmission paths. The closeness of the accelerometer to the transmission path also affects the signal energy.

4.2 Amplitude of the raw vibration data in time domain

The amplitude of the raw vibration signal of the baseline condition at 14000 rpm/ 100 KW from the four accelerometers was analyzed in the time domain and the outcome is summarized in Fig. 4. The data from the X channels of the two triaxial accelerometers was not considered since the impact of the planetary stages is most in the radial (-y) and tangential (-z) direction representing the Y and Z channel, respectively, and inconsequential in the axial (-x) direction. Hence, the X channel is not a sensitive vibration axis and was not considered suitable for signal analysis and fault diagnosis. The data collected from the triaxial accelerometer 1 positioned in the forward module has the highest amplitude of vibration both in the Y and Z channel. However, considering the location of this accelerometer to the incipient fault, the transmission path is longer compared to the other accelerometers position and is also not a direct path as it has to pass through several components in the MGB as shown in Fig. 2 and Fig. 3. The high amplitude in these channels might be due to the contributions of the parallel axis gears in the forward, aft and bevel reduction stages. Considering the data from the triaxial accelerometer 2 positioned in between the two epicyclic stages, the amplitude of vibration in the Y and Z channels are high enough though relatively less compared to that of triaxial accelerometer 1 positioned in the forward module. Also, the signals from the triaxial accelerometer 1 have less input from the forward, bevel, and aft reduction stages. The data recording from the uniaxial accelerometer 1 exhibits similar vibration amplitude and can be relatively compared to channels Y and Z of the triaxial accelerometer 1 positioned in the epicyclic module. Similar to the signals from the triaxial accelerometer 2, the uniaxial accelerometer 1 has a short transmission path and less interference from the forward, aft and bevel reduction stages. The uniaxial accelerometer 2 has a short transmission path like the triaxial accelerometer 2 and uniaxial accelerometer 1, however, it does not have a distinct signal amplitude, hence, it is not suitable for signal analysis.

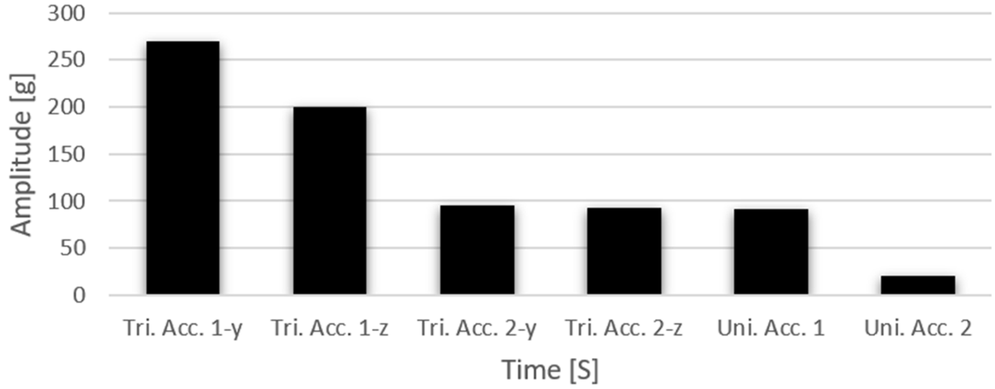

Fig. 4. Amplitude spectrum of the accelerometer channels.

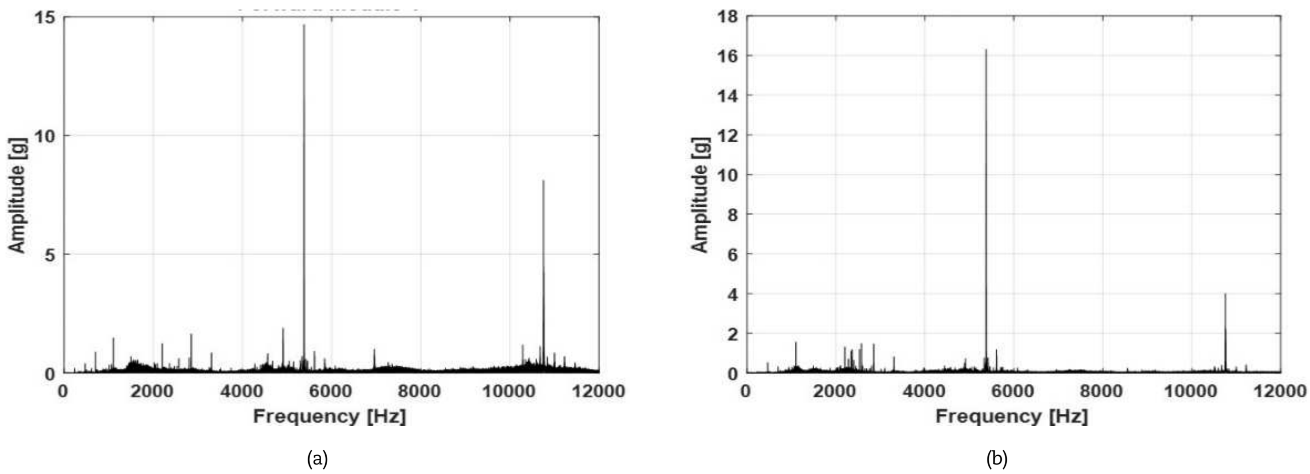

Fig. 5. Frequency spectrum of triaxial accelerometer 1 (a) channel Y (b) channel Z.

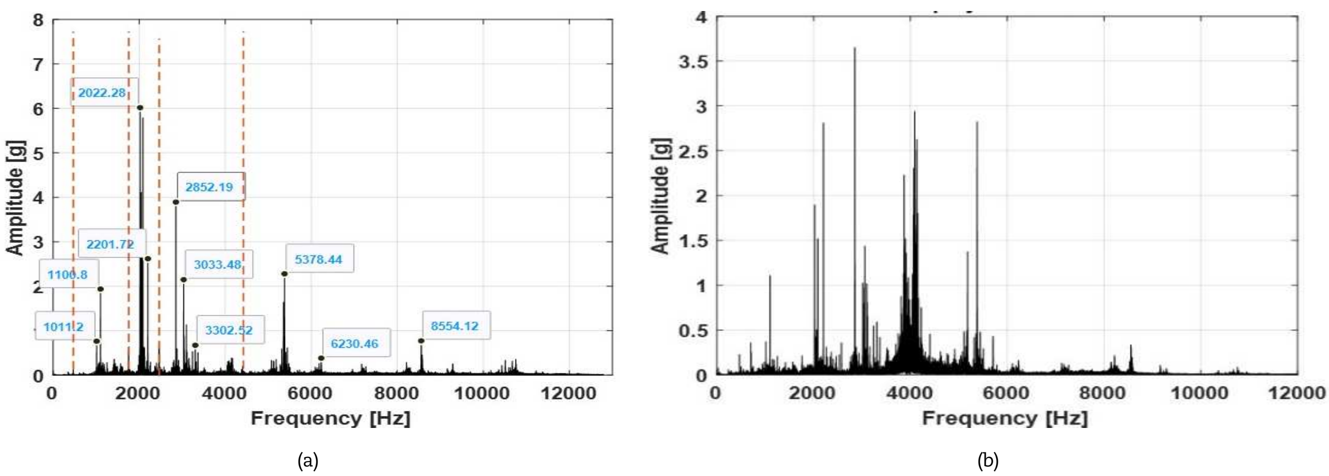

Fig. 6. Frequency spectrum of triaxial accelerometer 2 (a) channel Y (b) channel Z.

4.3 Frequency spectrum of the vibration signal

The vibration signals from the accelerometers are examined in the frequency domain to further investigate and establish the sensitive vibration axis. It has been shown in the previous section that the epicyclic motion of the planetary bearing has less impact in the axial (-x) direction, hence, the vibration signals from channel X for the two triaxial accelerometers will not be examined in this section. Fig. 5 shows the predominantly high amplitude of shaft and gear related frequency, especially from the forward modules picked along the transmission paths from the epicyclic module to channel Y and Z of the triaxial accelerometer 1 at the forward module. The high amplitude of the gear frequencies will suppress the frequency of interest from the epicyclic module, and more processing will be required, which may be time consuming and futile. Hence, the data from the forward module channels is not optimal for signal analysis, but, however, it could be very helpful in providing clear resonance of the assembly. The vibration signal of channel Y and Z of the triaxial accelerometer 2 positioned in the epicyclic module are presented in Fig. 6. These channels have distinct frequency characteristics with less interference from shaft and gear related frequencies from the forward, aft and bevel reduction stages. The frequency spectrum of the data from the uniaxial accelerometer 1, as shown in Fig. 7(a), exhibits similar frequency amplitude and relativity compared to channel Y of triaxial accelerometer 2, while the uniaxial accelerometer 2 located in the epicyclic module shows a very low signal amplitude with high noise peaks as shown in Fig. 7(b).

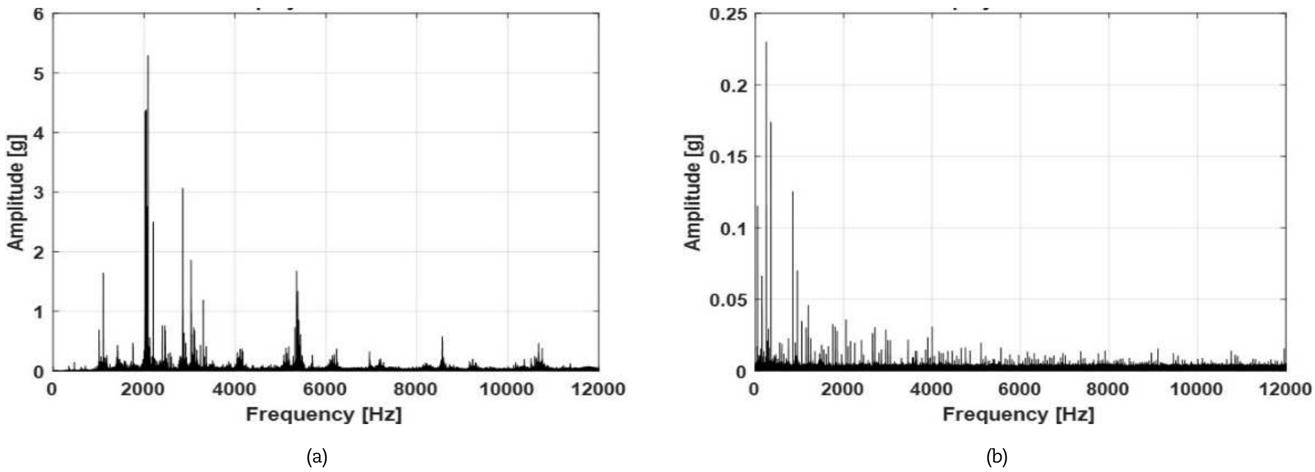

Fig. 7. Frequency spectrum of uniaxial accelerometer (a) acc-1 (b) acc-2.

From the observation of the three criteria for selection of the sensitive vibration axis the Y and Z channels of triaxial accelerometer 2 and the vibration signal of uniaxial accelerometer 1 are a better choice. These three channels have a straightforward transmission path as shown in Fig. 6 and Fig. 7, and relatively superior amplitude and frequency spectrum. Analyzing the frequency spectrum narrows the choice to channel Y of the triaxial accelerometer 2 and is considered as the most sensitive axis with superior frequency amplitude and data quality. Hence, the data from channel Y of the triaxial accelerometer 2 located at the epicyclic module will be most suitable for subsequent analysis and fault diagnosis. Channel Z of the triaxial accelerometer 2 and the data of uniaxial accelerometer 1 could be useful for extracting some vital information for signal processing such as GMF of the reduction stages, integer harmonics and resonance that may not be visible in Channel Y of the triaxial accelerometer 2.

4.4 Fundamental GMF, harmonics and planets modulation

Slight variation can be seen in the estimated values of the GMF, and its integer harmonics shown in Table 3 and the actual values in the frequency spectrum as shown in Fig. 6. This deviation is a result of the slight variation in the operational speed of the MGB and bearing roller slips experienced during operation. The fundamental GMF and integer harmonics of the 1st and 2nd epicyclic stages have been shown in Table 3 and can be identified in the frequency spectrum in Fig. 6. The prominent GMF and their harmonics present in the spectrum are largely due to the vibration input of the fixed axis gears and modulated by the planetary gears. Some other visible frequency components other than the GMF and harmonics which are due to the modulations of the planetary stages caused by bearing slip or gear modulations; and are either an addition or subtraction of some other frequency values. It can be observed from Fig. 6 that the dominant frequency components of the planetary stages are suppressed in the spectrum by the modulating sidebands and high frequency of the FRG, ARG and BRG. This is with the exception of the 5th harmonics of the 2nd planetary stage, and the 8th harmonics of the 1st planetary stage which can be seen in the frequency spectrum. The other dominant frequency components in the spectrum are related to the input speed or the GMF of the FRG, ARG and BRG or their modulation by the planetary gears. For instance, 467.7 Hz corresponds 2nd harmonics of the input speed (233.33 Hz) of the FRG. 1101, 2203, 3303, and 4403 correspond to the GMF of the BRG and its 2nd, 3rd, and 4th harmonics. 2852 Hz is the GMF of the ARG, while 5378 Hz is the GMF of the FRG. It is clearly seen that the GMF and integer harmonics of the planetary stages are suppressed in the spectrum because of the amplitude modulated signal of the planetary stage caused by the similar vibration behavior of the planet gears operating at the same speed and load but different and changing meshing faces. Hence, the dominant frequency component of the planetary stage is asymmetric to the GMF and become suppressed in the spectrum. Also, the ratio of the ring gear teeth (Z_r) to the number of planet gears (n_p) of the two epicyclic stages is a fraction (i.e., 130/8 and 130/9) and not an integer, which is a condition for high amplitudes. In addition, the vibration transmission paths from the meshing of the planet gears with the sun and ring to the accelerometers due to the planet carrier rotation and the constantly changing meshing phase of the planet gears imposed planet modulation on the vibration signal and greatly impacted the vibration energy level as the frequency spectrum of the signal will be dominated by FRG, ARG, and BRG since the 1st and the 2nd planetary stage naturally have low vibration energy.

Figure 9(a) presents the zoomed amplitude spectrum showing the sun gear speed of the 1st planetary stage (24.38 Hz) modulated by the integer multiples of the carrier speed of the 2nd planetary stage (2.7 Hz) spread across the frequency band. The modulated frequencies also exist around the region of the fault frequencies, and this could be challenging to fault diagnosis in the planetary MGB.

4.5 Determination of the carrier frequency

The bearing carrier frequency should have no strong correlation with the gear and shaft related frequencies and should be within the region of 12800 Hz theoretically. The carrier frequency is an essential factor for bearing envelope analysis in the selection of the demodulating frequency band for effective fault extraction. The fast kurtogram [42] has proven to be an efficient algorithm for extracting this impulsive frequency and the demodulating bandwidth. However, the kurtogram fail to indicate the carrier frequency and the optimal bandwidth for demodulation in a complex gear arrangement [45-45]. Hence, the outcome of the investigation using the fast kurtogram are not considered in this study.

Figure 8 present the carrier frequency for the 14000 rpm/ 100 kW, 14000 rpm/ 180 kW, 16000 rpm/ 100 kW and 16000 rpm/ 180 kW load regime manually selected from the spectrum. For the low speed regime at 14000 rpm, as observed in Fig. 8(a) and Fig. 8(b), the carrier frequency should be the peak of a dumbbell shape within the region of halve of the sampling frequency, however, the closest to the theoretical value within that region in the spectrum is 10800 Hz. The variation in the theoretical value and actual value of the carrier frequency in the spectrum maybe attributed to the variation in the operational speed of the MGB, bearing roller slips, the complex structure of the planetary gear set and manufacturing variation. For the high-speed regime at 16000 rpm, as shown in Fig. 8(c) and Fig. 8(d), the estimated carrier frequency, which is about approximately half of the sampling frequency, is not the highest point in the region around 10000. It is actually about the lowest point, while the highest point in this region is close to the 8th harmonics of the 1st planetary stage carrier. Hence there is the likelihood of gear interference due to a strong correlation with gear frequencies and could mitigate fault diagnosis.

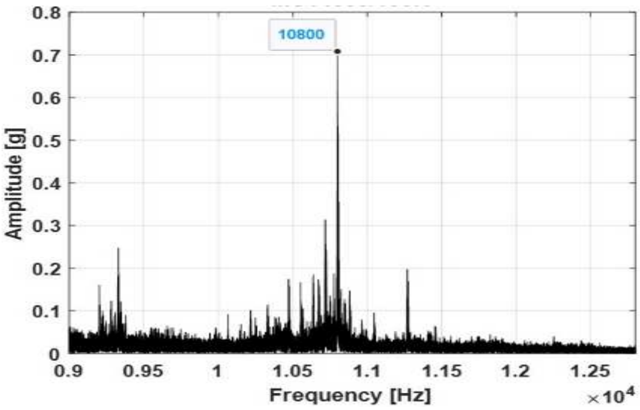

(a)

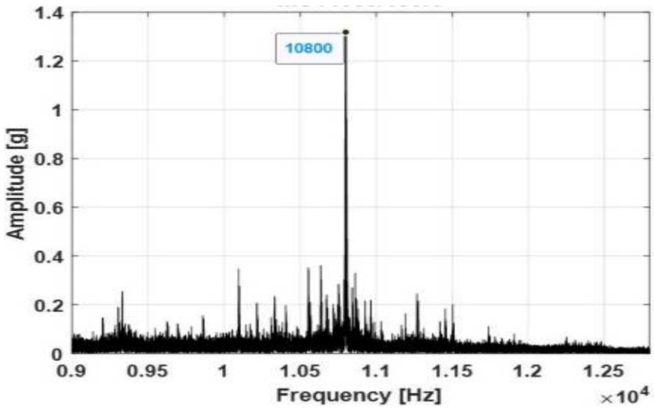

(b)

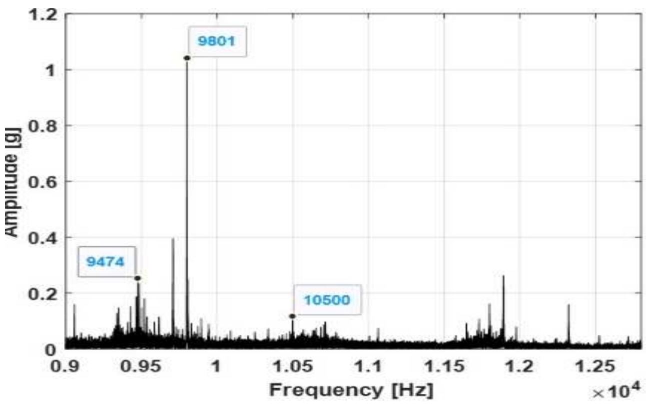

(c)

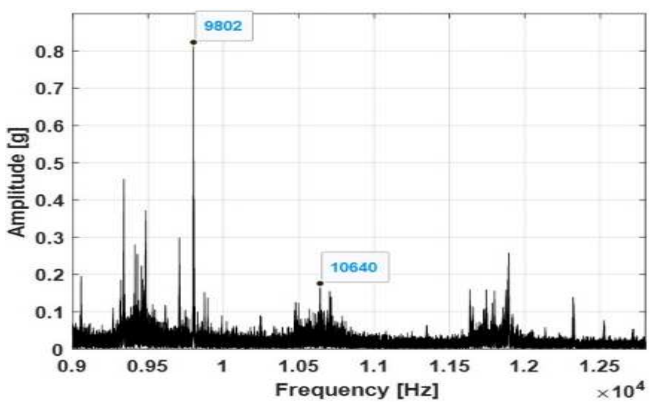

(d)

Fig. 8. Carrier frequency for (a) 14000 rpm/100 kW (b) 14000 rpm/180 kW (c) 16000 rpm/100 kW (d) 16000 rpm/ 180 kW.

4.6 Preliminary demonstration of the fault frequencies

This section presents a preliminary illustration of the fault frequencies as a precursor for further fault diagnosis. The estimated BPFO, L_S and U_S sidebands are presented in Tables 4 and 5 for 14000 rpm and 16000 rpm loading regimes. From the estimated values of the BPFO and its sideband, their values are between 65 and 72 Hz. Hence, the focus of the analysis will lie in the region of 0 to 100 Hz. The presence of frequencies not associated with bearing outer race faults can be seen as high spikes in Fig. 9 for the baseline, mild fault, and severe fault conditions, respectively, for both the 14000 rpm/ 100 kW and 14000 rpm/180 kW load regime. The frequencies 24.44 Hz, 43.40 Hz and 48.87 Hz present in all three conditions are gear related frequencies of the 1st and 2nd planetary stage modulating the planetary carrier of the 2nd planetary stage, its 2nd harmonics and the sun gear speed of the 1st planetary stage modulated by the 2nd planetary carrier. For the baseline condition, there are no indications of the BPFO, L_S and U_S, as shown in Fig. 9(a). However, the presence of gear related frequency was noticed around the region of the BPFO as 59.72 Hz corresponding to the modulation of the 2nd planetary stage carrier by some integer multiples. Likewise, gear related frequencies are evident around the region of the upper sideband of the BPFO.

For the mild fault condition of 14000 rpm/ 100 kW load regime in Fig. 9(b), the BPFO is not present, but its L_S and U_S appear as 57.21 Hz and 62.72 Hz, respectively, while in Fig. 9(c), the severe fault condition of 14000 rpm/ 100 kW load regime shows indications of the BPFO, L_S and U_S as 60.05 Hz, 57.33 Hz and 62.77 Hz, respectively. Fig. 9(d) shows the mild fault condition for the 14000 rpm/180 kW load regime. There is no indication of the BPFO in the spectrum, however, the fault related sidebands, the L_S and U_S are obvious and can be seen in the spectrum as 57.21 Hz and 62.62 Hz, respectively. Likewise, there is no obvious BPFO in the severe fault condition for the 14000 rpm/ 180 kW load regime, as shown in Fig. 9(e), but the U_S is obvious and appears as 62.77 Hz, while the L_S is suppressed in the spectrum by gear related frequencies. The overwhelming influence of the gear related frequencies of the 1st and 2nd epicyclic stage of the MGB is obvious in the baseline condition, mild fault condition and severe fault condition for both load regimes.

Table 4. Parameters of the 14000 rpm loading regime.

	Baseline condition	Mild fault condition	Sever fault condition
Speed (rpm)	14034	14088	14120
1st Carrier	7.90	7.93	7.95
2nd Carrier	2.71	2.72	2.73
BPFO (Hz)	-	59.67	59.81
Ls (HZ)	-	56.95	57.08
Us (Hz)	-	62.39	62.54

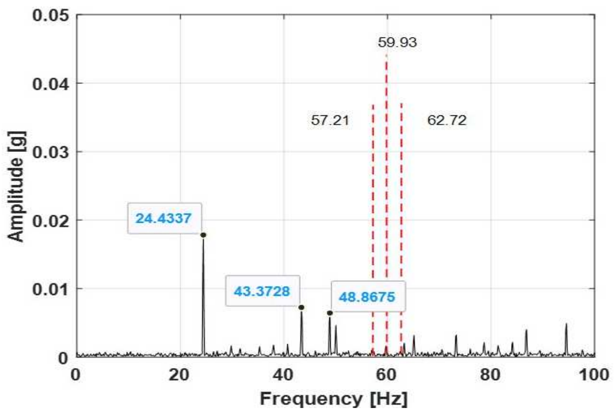

(a)

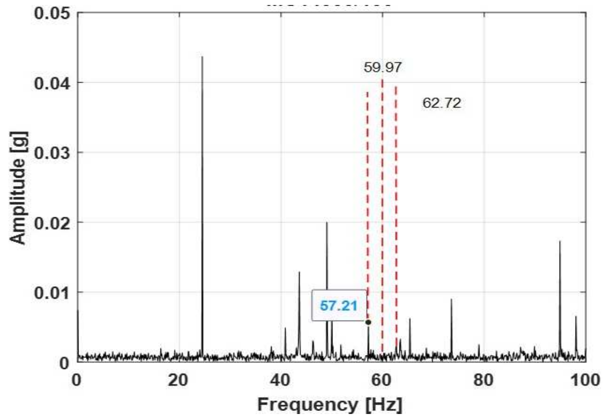

(b)

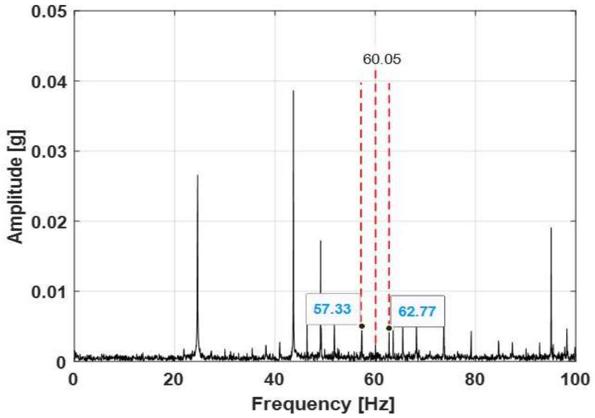

(c)

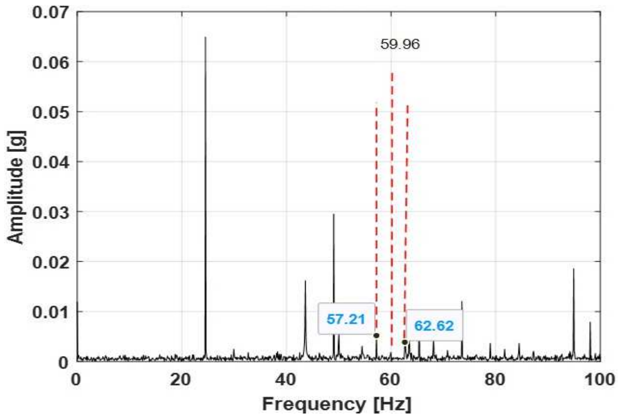

(d)

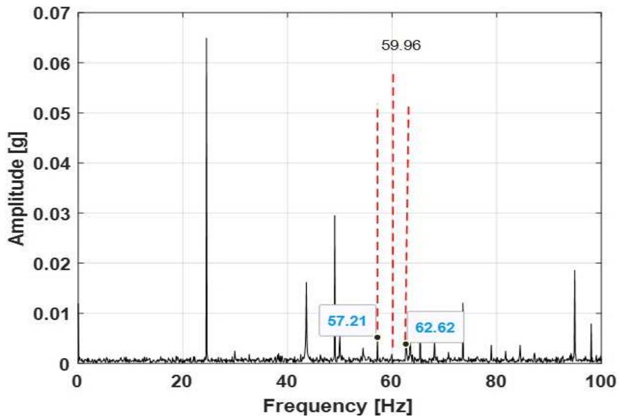

(e)

Fig. 9. Zoomed amplitude spectrum at 14000 rpm (a) baseline condition (b) mild fault at 100 kW (c) severe fault at 100 kW (d) mild fault at 180 kW (e) severe fault at 180 kW.

Table 5. Parameters of the 16000 rpm loading regime.

	Baseline condition	Mild fault condition	Sever fault condition
Speed (rpm)	16038	16074	16110
1st Carrier	9.03	9.05	9.07
2nd Carrier	3.1	3.11	3.12
BPFO (Hz)	-	68.08	68.24
Ls (HZ)	-	64.97	65.21
Us (Hz)	-	71.19	71.36

The baseline condition for 16000 rpm load regime is shown in Fig. 10(a), with no sign of the BPFO nor any of L_S and U_S. Likewise, the mild fault condition for 16000 rpm/ 1000 kW shown in Fig. 10(b) shows no sign of the BPFO, however, the lower sideband of the BPFO is indicated in the frequency spectrum, while the upper sideband is subdued. Figure 10(c) shows the frequency spectrum of the severe fault condition for the 16000 rpm/100 kW load regime. There is a clear indication of the planetary bearing fault frequencies, the BPFO, L_S and U_S of the BPFO. The lower and upper sideband of the BPFO is indicated in the mild fault condition, while the BPFO is clouded in the spectrum in Fig. 10(d) for the 16000 rpm/ 180 kW load regime, while for the severe fault condition under the same load regime in Fig. 10(e), all the planetary bearing fault frequencies, the BPFO, lower and upper sideband of the BPFO are all indicated.

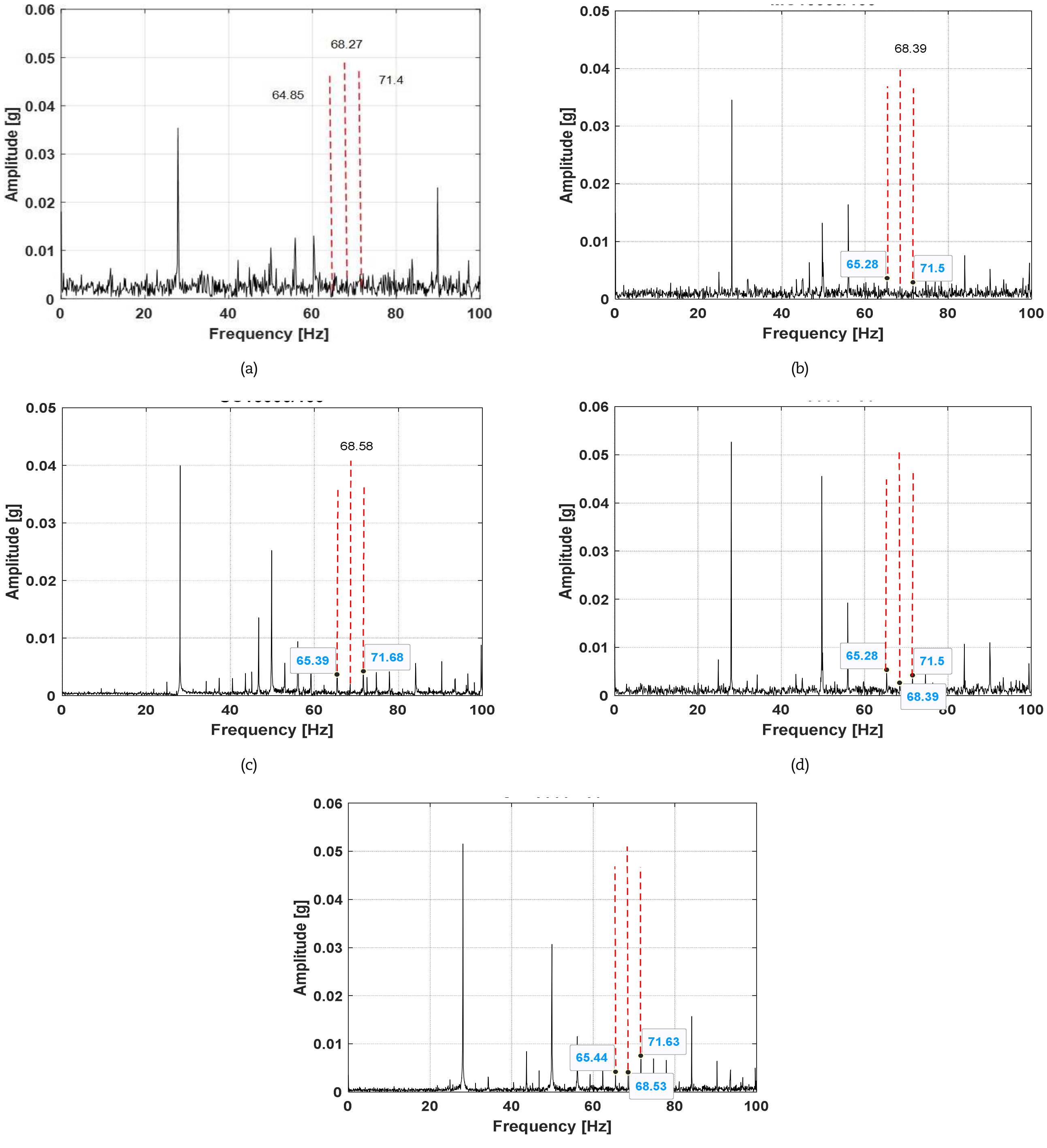

Fig. 10. Zoomed amplitude spectrum at 16000 rpm (a) baseline condition (b) mild fault at 100 kW (c) severe fault at 100 kW (d) mild fault at 180 kW (e) severe fault at 180 kW.

Slight variation can be seen in the estimated values of the BPFO, its lower and upper sideband as shown in Tables 4 and 5 and the actual values in the amplitude spectrum as shown in Fig. 9 and Fig.10. This deviation is a result of the slight variation in the operational speed of the MGB and bearing roller slips experienced during operation. The variation also affects the actual and estimated values of other frequencies, as seen in the case of the gear related frequencies 24.44 Hz, 43.40 Hz and 48.87 Hz corresponding to the 9th planetary gear of the 2nd planetary stage modulating the planetary carrier of the 2nd planetary stage, its 2nd harmonics and the sun gear speed of the 1st planetary stage modulated by the 2nd planetary carrier.

As can be seen for all the loading regimes, the effect of gear related frequencies from the 1st and 2nd epicyclic stages not relating to the fault frequencies is predominant in the spectrum for the baseline, mild fault, and severe fault conditions. These gear related frequencies mitigate the diagnosis of the fault frequencies, which are buried in the gear dominated spectrum. It will be essential to extract the fault related frequencies so that BPFO and the fault related sidebands are without the interferences from other dominant shaft and gear mesh frequencies.

5. Conclusion

This study examined the vibration data of mild and severe fault seeded in the outer race of a planetary bearing of the second stage epicyclic stage of SA 330 MGB under varying load regimes collected over eight channels with two uniaxial and two triaxial accelerometers. The choice of the sensitive vibration axis was premised on the vibration transfer path, amplitude spectrum and frequency spectrum. Though the bearing fault frequencies can be seen in some cases in the spectrum but are dominated by gear related frequencies of the single-axis gears and the planetary stages. The amplitude-modulating sidebands of the planetary stage had significant effect on the frequency spectrum. Likewise, the high frequency of the single axis gears further suppressed the prominent frequency components and their integer harmonics. Aside the 5^{th} and 7^{th} harmonics of the 2^{nd} planetary stage, and the 6^{th} and 8^{th} harmonics of the 1^{st} planetary stage, all other frequency components and their harmonics were suppressed in the spectrum. Modulating sidebands of the planetary stages such as 1011, 1998, 3041, 3112, and 5417 Hz were also noticeable in the spectrum. Likewise, frequencies related to the input speed or the GMF of the FRG, ARG and BRG or their modulation by the planetary gears were dominant in the spectrum and appears as 467.7, 1101, 2203, 2852, 3303, 4403, and 5378 Hz. The bearing carrier frequency was low and had a strong correlation with gear related frequencies at high speed compared to a low speed. The study proposed novel analysis of the data quality for the future fault diagnostics. The effect of some necessary parameters for fault diagnosis were investigated. Though the study employed FFT as a preliminary investigation, however, for adequate fault extraction, further work is required. Future work should focus on the investigation and diagnosis of the fault frequencies with advanced frequency domain techniques and the comparative study of the performance of the data channels.

Author Contributions

All authors contributed to the study. Material preparation, data collection and analysis were performed by A.A. Ogundare, S.J. Ojolo, D. Mba, and L. Zhou. A.O. Adelaja and X. Li contributed to the data analysis and the manuscript. The first draft of the manuscript was written by A.A. Ogundare and all authors commented on previous versions of the manuscript. All authors discussed the results, reviewed and approved the final version of the manuscript.

Acknowledgments

The authors, S.J. Ojolo, D. Mba and A.A. Ogundare wish to acknowledge the Tertiary Education Trust Fund (TETFUND) for supporting the research through the Grant Award NRF/STI/37.

Conflict of Interest

The authors declared no potential conflicts of interest concerning the research, authorship, and publication of this article.

Funding

The authors, S.J. Ojolo, D. Mba and A.A. Ogundare received financial support from the Tertiary Education Trust Fund (TETFUND) through the Grant Award NRF/STI/37.

Data Availability Statements

The datasets generated and/or analyzed during the current study are available from the corresponding author on reasonable request.

Nomenclature

ARG	Aft Reduction Gear	N_{O1}	Output speed of the 1st planetary stage
BRG	Bevel Reduction Gear	N_{O2}	Output speed of the 1st planetary stage
FRG	Forward Reduction Gear	N_P	Speed of the planetary gears
GMF	Gear Mesh Frequency	R_F	Gear transmission ratio of the Forward reduction stage
MGB	Main gearbox	R_A	Gear transmission ratio of the Aft reduction stage
R	Transmission ratio	R_B	Gear transmission ratio of the Bevel reduction stage
F_P	Fundamental Gear mesh frequency of the planetary stage	R_{p1}	Gear transmission ratio of the 1st planetary stage
GMF_F	Gear mesh frequency of the forward reduction stage	R_{p2}	Gear transmission ratio of the 2nd planetary stage
GMF_A	Gear mesh frequency of the aft reduction stage	Z_r	Number of teeth of the ring gear
GMF_B	Gear mesh frequency of the bevel reduction stage	Z_S	Number of teeth of the sun gear
H_i	Integer harmonics of the planetary stage	Z_p	Number of teeth of the planet gears
n_i	Index number of the planetary gear	Z_{PF}	Number of pinion teeth on the forward reduction stage
N_i	Input speed from the engine	Z_{SF}	Number of spur teeth on the forward reduction stage
N_{OF}	Output speed of the Forward reduction gear	Z_{PA}	Number of pinion teeth on the aft reduction stage
N_{OA}	Output speed of the Aft reduction gear	Z_{PB}	Number of pinion teeth on the bevel reduction stage
N_{OB}	Output speed of the Bevel reduction gear	Z_{SA}	Number of spur teeth on the aft reduction stage

References

[1] Mosher, M., Understanding vibration spectra of planetary gear systems for fault detection, *ASME DETC/CIE*, 37025, 2003, 645-652.
[2] Lei, Y., Han, D., Lin, J., He, Z., Planetary gearbox fault diagnosis using an adaptive stochastic resonance method, *Mechanical Systems and Signal Processing*, 38(1), 2013, 113–124.
[3] Tica M., Vrcan Ž., Troha S., Marinković D., Reversible Planetary Gearsets Controlled by Two Brakes, for Internal Combustion Railway Vehicle Transmission Applications, *Acta Polytechnica Hungarica*, 19(10), 2022, 95-108.
[4] Marghitu, D.B., *Kinematic chains and machine components design*, Elservier Academic Press, Oxford, 2005.
[5] Constans, E., Dyer, K.B., *Introduction to mechanism of the design with computer applications*, CRC Press, Taylor and Francis Group, Boca Raton, 2019.
[6] Lei, Y., Lin, J., Zuo, M. J., He, Z., Condition monitoring and fault diagnosis of planetary gearboxes: A review, *Measurement*, 48(1), 2014, 292–305.

[7] Blunt, D.M., Keller, J.A., Detection of a fatigue crack in a UH-60A planet gear carrier using vibration analysis, *Mechanical Systems and Signal Processing*, 20(8), 2006, 2095–2111.
[8] Grabill, P., Keller, J., Vibration Monitoring of UH-60A Main Transmission Planetary Carrier Fault, *AHS 59th Annual Forum*, 9(2), 2003, 1233-1243.
[9] Lewicki, D.G., LaBerge, K.E., Ehinger, R.T., Fetty, J., Planetary gearbox fault detection using vibration separation techniques, *VFS 67th Annual Forum and Technology Display*, E-17816 4, 2011, 2489–2502.
[10] Lei, Y., Kong, D., Lin, J., Zuo, M.J., Fault detection of planetary gearboxes using new diagnostic parameters, *Measurement Science and Technology*, 23(5), 2012, 055605.
[11] Saxena, A., Wu, B., Vachtsevanos, G., A methodology for analyzing vibration data from planetary gear systems using complex morlet wavelets, *Proceedings of the 2005, American Control Conference*, 7, 2005, 4730–4735.
[12] Mosher, M., Results from a new separation algorithm for planetary gear system vibration measurements, *ASME DETC/CIE,* 5, 2005, 747–754.
[13] Lei, Y., Liu, Z., Lin, J., Lu, F., Phenomenological models of vibration signals for condition monitoring and fault diagnosis of epicyclic gearboxes, *Journal of Sound and Vibration*, 369, 2016, 266–281.
[14] Sawalhi, N., Vibration sideband modulations and harmonics separation of a planetary helicopter gearbox with two different configurations, *Advances in Acoustics and Vibration*, 2016, 2016, 9820768.
[15] Feng, Z., Zuo, M.J., Vibration signal models for fault diagnosis of planetary gearboxes, *Journal of Sound and Vibration*, 331(22), 2012, 4919-4939.
[16] Litt, J.S., Simon, D.L., Garg, S., Guo, T.H., Mercer, C., Millar, R., Behbahani, A., Bajwa, A., Jensen, D.T., A survey of intelligent control and health management technologies for aircraft propulsion systems, *Journal of Aerospace Computing, Information, and Communication*, 1(12), 2004, 543-563.
[17] Siegel, D., Ly, C., Lee, J., Methodology and framework for predicting helicopter rolling element bearing failure, *IEEE Transactions on Reliability*, 61(4), 2012, 846–857.
[18] Samuel, P.D., Conroy, J.K., Pines, D.J., Planetary Transmission diagnostics, *NASA/TM-* 20040073522, 2004.
[19] Kiddy, J.S., Samuel, P.D., Lewicki, D.G., Ehinger, R.T., LaBerge, K.E., Fetty, J., Fiber optic strain sensor for planetary gear diagnostics, *AHS 67th Annual Forum and Technology Display*, 2011, 2396–2411.
[20] Greaves, M., Elasha, F., Worskett, J., Mba, D., Rashid, H., Keong, R., Vibration health or alternative monitoring technologies for helicopters, *EASA Technical Report*, 2017.
[21] Sawalhi, N., Randall, R.B., Simulating gear and bearing interactions in the presence of faults. Part I. The combined gear bearing dynamic model and the simulation of localised bearing faults, *Mechanical Systems and Signal Processing*, 22(8), 2008, 1924–1951.
[22] Lewicki, D.G., Coy, J.J., Helicopter Transmission Testing at Nasa Lewis Research Center, *NASA/TM-89912*, 1987.
[23] Lewicki, D.G., Coy, J.J., Vibration characteristics of OH-58A helicopter Main Rotor Transmission, *NASA Cleveland OH Lewis Research Center*, 1997.
[24] Hardman, W., Hess, A., Blunt, D., A USN development strategy and demonstration results for propulsion and mechanical systems diagnostics, prognostics, and health management, *IEEE Aerospace Conference Proceedings*, 6, 2001, 63059–63068.
[25] Keller, J., Grabill, P., Inserted fault vibration monitoring tests for a CH-47D Aft swashplate bearing, *AHS 61st Annual Forum*, 2005.
[26] Decker, H.J., Lewicki, D.G., Spiral bevel pinion crack detection in a helicopter gearbox, *NASA, Cleveland OH Glenn Research Center,* 2003.
[27] Delgado, I.R., Dempsey, P.J., Simon, D.L., A Survey of Current Rotorcraft Propulsion Health Monitoring Technologies, *NASA/TM* -217420, 2012.
[28] Simon, D.L., Garg, S., Hunter, G.W., Guo, T.H., Semega, K.J., Sensor needs for control and health management of intelligent aircraft engines, *Turbo Expo: Power for Land, Sea and Air,* 41677, 2004, 873–882.
[29] Greaves, M., Elasha, F., Worskett, J., Mba, D., Rashid, H., Keong, R., Vibration health or alternative monitoring technologies for helicopters, *EASA Technical Report*, 2017.
[30] Dempsey, P.J., Branning, J., Wade, D.R., Bolander, N., Comparison of test stand and helicopter oil cooler bearing condition indicators, *AHS 66th Annual Forum and Technology Display,* 1, 2010, 597–605.
[31] Dempsey, P.J., Mosher, M., Huff, E.M., Threshold Assessment of Gear Diagnostic Tools on Flight and Test Rig Data, 59th *Annual Forum and Technology Display*, 2003.
[32] Mosher, M., Pryor, A.H., Huff, E.M., Evaluation of standard gear metrics in helicopter flight operation, *56th Meeting of the Society of Machinery Failure Prevention Technology*, 2002.
[33] Wang, T., Han, Q., Chu, F., Feng, Z., Vibration based condition monitoring and fault diagnosis of wind turbine planetary gearbox: A review, *Mechanical Systems and Signal Processing*, 126, 2019, 662-685.
[34] Jing, L., Wang, T., Zhao, M., Wang, P., An adaptive multi-sensor data fusion method based on deep convolutional neural networks for fault diagnosis of planetary gearbox, *Sensors*, 17(2), 2017, 414.
[35] Yang, Z., Wang, S., Ma, C., Huang, J., Development of fault diagnosis system for wind power planetary transmission based on labview, *The Journal of Engineering*, 23, 2019, 9170-9172.
[36] Algin, V., Ishin, M., Paddubka, S., Models and approaches in design and diagnostics of vehicles planetary transmissions, *IOP Conference Series: Materials Science and Engineering*, 393(1), 2018, 012042.
[37] Troha, S., Vrcan, Ž., Karaivanov, D., Isametova, M., The selection of optimal reversible two-speed planetary gear trains for machine tool gearboxes, *Facta Universitatis-Series Mechanical Engineering*, 18(1), 2020, 121-134.
[38] Azzam, B., Schelenz, R., Jacobs, G., Sensor Screening Methodology for Virtually Sensing Transmission Input Loads of a Wind Turbine Using Machine Learning Techniques and Drivetrain Simulations, *Sensors*, 22(10), 2022, 3659.
[39] Hess, R., Duke, A., Kogut, D., The IMD HUMS as a tool for rotorcraft health management and diagnostics, *IEEE Aerospace Conference Proceedings*, 6, 2001, 3039-3058.
[40] Mosher, M., Pryor, A.H., Lewicki, D.G., Detailed vibration analysis of pinion gear with time-frequency methods, NASA/TM- 47, 2003.
[41] Ho, D., Randall, R.B., Effects of Time Delay, Order of FIR filter and convergence factor on self-adaptive noise cancellation, *5th International Congress of Sound and Vibration*, 1997, 945–52.
[42] Antoni, J., Fast computation of the kurtogram for the detection of transient faults, *Mechanical Systems and Signal Processing*, 21(1), 2007, 108-124.
[43] Dong, W., Tse, P.W., Tsui, K.L., An Enhanced Kurtogram Method for Fault Diagnosis of Rolling Element Bearings, *Mechanical Systems and Signal Processing*, 35(1–2), 2013, 176–99.
[44] Zhou, L., Duan, F., Mba, D., Wang, W., Ojolo, S., Using frequency domain analysis techniques for diagnosis of planetary bearing defect in a CH-46E helicopter aft gearbox, *Engineering Failure Analysis*, 92, 2018, 71-83.
[45] Zhou, L., Duan, F., Corsar, M., Elasha, F., Mba, D., A study on helicopter main gearbox planetary bearing fault diagnosis, *Applied Acoustics*, 147, 2019, 4-14.

ORCID iD

A.A. Ogundare https://orcid.org/0000-0003-3523-8214
S.J. Ojolo https://orcid.org/0000-0002-4548-0090
A. Adelaja https://orcid.org/0000-0001-9175-8332
D. Mba https://orcid.org/0000-0001-7278-4623
L. Zhou https://orcid.org/0000-0003-3502-1832
X. Li https://orcid.org/0000-0002-5494-1266

How to cite this article: Ogundare A.A., Ojolo S.J., Adelaja A., Mba D., Zhou L., Li X. Study of the Vibration Characteristics of SA 330 Helicopter Planetary Main Gearbox, *J. Appl. Comput. Mech.*, 9(4), 2023, 1093–1106.
https://doi.org/10.22055/jacm.2023.43103.4028